Ti$_3$C$_2$T$_x$ Electromagnetic Shielding Performance: Investigating Environmental Influences and Structural Changes

Arturo Barjola, Roberto Herráiz, Andrea Amaro, José Torres,* Adrián Suárez, and Enrique Giménez*

MXenes, a promising family of 2D transition metal carbides/nitrides, are renowned for their exceptional electronic conductivity and mechanical stability, establishing them as highly desirable candidates for advanced electromagnetic interference (EMI) shielding material. Despite these advantages, challenges persist in optimizing MXene synthesis methods and improving their oxidation resistance. Surface defects on MXenes significantly impact their electronic properties, impeding charge transport and catalyzing the oxidation process. In this study, a novel synthesis protocol derived from the conventional, minimally invasive layer delamination (MILD) method, is presented. Two additional steps are introduced aiming at enhancing process yield, addressing a crucial issue as conventional methods often yield high-quality individual MXene flakes but struggle to generate sufficient quantities for bulk material production. This approach successfully yields Ti$_3$C$_2$T$_x$ films with excellent conductivity (3973.72 $\pm$121.31 Scm^{-1}) and an average EMI shielding effectiveness (SE) of 56.09 $\pm$ 1.60 dB within the 1.5 to 10 GHz frequency range at 35% relative humidity (RH). Furthermore, this investigation delves into the long-term oxidation stability of these films under varying RH conditions. These findings underscore the effectiveness of this innovative synthesis approach in elevating both the conductivity and EMI shielding capabilities of MXene materials. This advancement represents a significant step toward harnessing MXenes for practical applications requiring robust EMI shielding solutions. Additionally, insights into long-term stability offer critical considerations for implementing MXenes in real-world environments.

1. Introduction

The increasing demand for reliable electronics and the rapid expansion of new telecommunications systems have underscored the critical importance of electromagnetic interference (EMI) shielding.[1,2] The advent of 5G communication and its associated technologies has opened pathways for numerous innovations in the communication industry. Consequently, ongoing efforts are focused on developing new EMI shielding materials capable of facilitating the co-existence of 5G with other technologies.

Investigations into lightweight EMI shielding materials are crucial for enhancing safety in 5G communications. Shielding effectiveness (SE) emerges as a critical parameter for material selection, defining the extent to which an electromagnetic wave is attenuated while passing through a medium A after interacting with a medium B (the shielding material).

The ASTM D4935-18 standard test method is commonly used to measure the electromagnetic SE of planar materials. However, this method is limited to a narrow frequency range (30 MHz

A. Barjola, E. Giménez
Instituto Universitario de Tecnología de Materiales
Universitat Politècnica de València
Camino de Vera s/n 46022, Valencia, Spain
E-mail: enrique.gimenez@mcm.upv.es

R. Herráiz, A. Amaro, J. Torres, A. Suárez
Escola Tècnica Superior d'Enginyeria
University of València (UV)
Avenida de la Universidad s/n
Burjassot 46100, Spain
E-mail: jose.torres@uv.es

to 1.5 GHz), rendering it inadequate for evaluating the SE of 5G technology, which operates at significantly higher frequencies.[3] To address this limitation, the upper-frequency limit of the ASTM D4935-18 standard can be extended by modifying the dimensions of the standard coaxial cell holder,[4–6] as employed in our measuring technique. While traditional metal shields effectively reduce EMI, they often exhibit drawbacks such as limited flexibility, high weight, large volume, and low corrosion resistance.[7,8] In contrast, magnetic material is an interesting solution due to its significant electromagnetic wave absorption capabilities and the ability to be mixed to form a polymeric sheet.[9–11] Carbon-based materials, including carbon nanotubes (CNTs) and graphene foams, with their unique properties of high electrical conductivity and low density, show promise for effectively absorbing electromagnetic waves.[12,13] Previous research has demonstrated that composite materials, particularly those incorporating carbon fibers or copper mesh, can significantly reduce EMI compared to conventional metals. The following results report an analysis of the low-frequency part of the 5G Frequency Range 1 (FR1). In the study of different rigid materials that contain various concentrations of CNTs, it was found that an ABS-15w%CNT composite sheet with a thickness of 2.1 mm demonstrated an attenuation value of 58.20 dB when tested at a frequency of 3.5 GHz.[14] Another study shows the measurement of two different composites based on combining carbon fiber with multi-walled carbon nanotubes (MWCNT) and introducing a copper mesh between carbon fiber films. The results showed that the attenuation was ≈54.80 dB at the frequency of 3.5 GHz for the CF-MWCNT (2.30 mm sheet thickness) scenario and a value of 64.30 dB for the sample of CF-Cu (2.45 mm sheet thickness), respectively.[15] A different research study examined how well carbon materials such as colloidal and flexible graphite or carbon fibers, perform in shielding against EMI. Specifically, a sample containing 20 vol% carbon fibers (2.80 mm thickness) composition exhibited an EMI SE of over 19 dB.[16]

MXenes, a novel class of 2D transition metal carbides/nitrides, exhibit outstanding electronic conductivity and can be easily fabricated into flexible films, making them excellent candidates for EMI shielding applications.[17] Among these, $Ti_3C_2T_x$ stands out for its highest conductivity within the MXene family and has been extensively studied for its effectiveness in shielding against EMI.[18] Typically synthesized by selectively etching the Al layer from the MAX phase (Ti_3AlC_2), resulting in surface functional groups denoted by T (-OH, -O, -F) during the acidic etching process, $Ti_3C_2T_x$ has exhibited remarkable performance as an EMI shielding material.[19] MXenes, known for their superior electronic conductivity, impart materials with a high density of free charges on their surface, enabling them to reflect electromagnetic (EM) waves effectively. However, these excellent conductive properties may lead to impedance mismatch effects, resulting in materials with poor EM wave absorption values, which are insufficient for mitigating environmental pollution caused by EM radiation.[20] Among the various strategies explored to achieve multifunctional EM shielding MXene materials that provide both reflection and absorption properties, the production of hierarchical architectures emerges as one of the most effective.[21] The development of MXene materials with tailored hierarchical architectures has been pursued through various methods, including self-assembly, template assistance, electrospinning, and dip coating methods, among others. Vacuum-assisted assembly stands out as a significant self-assembly method conducive to obtaining multilayer MXene films capable of enhancing absorption performance. Recently, Shahzad et al.[22] demonstrated the potential of $Ti_3C_2T_x$ through the fabrication of ultra-thin films ≈2.5 µm thick. Exploiting the exceptional conductivity of MXene (4600 Scm⁻¹), these films exhibited an EMI SE exceeding 50 dB outperforming all known synthetic materials at comparable thicknesses. Furthermore, their study highlighted the dominance of absorption over reflection as the primary mechanism in the shielding process.

W-T. Cao et al.[23] fabricated an ultrathin, mechanically robust composite paper based on $Ti_3C_2T_x$ and cellulose nanofibers (CNFs), measuring 47 µm thickness. The strong interaction observed between the MXene sheets and the 1D CNF in the nacred-like structure endowed the MXene-based material with outstanding mechanical properties. The as-prepared composite paper exhibited a considerable conductivity value of 739.4 S m⁻¹ at 90 wt% of $Ti_3C_2T_x$ content. When the MXene content was reduced to 80 wt%, the composite paper achieved an EMI shielding value of ≈25.8 dB at 12.4 GHz. Concerning the SE mechanism of the composite paper, it can be concluded that absorption, rather than reflection, was the primary parameter contributing to the total SE. S. Yang et al.[24] prepared a multilayer film based on alternating layers of aramid nanofibers/polypyrrole nanowires (AFPy) and $Ti_3C_2T_x$ reinforced by waterborne polyurethane ($Ti_3C_2T_x$@WPU). The film, containing 32 wt% of MXene content, exhibited a remarkable EMI SE of 40.9 dB, primarily attributed to the improved absorption capacity of the layered $Ti_3C_2T_x$-based material. However, the chemical stability of MXenes in the presence of water and oxygen remains a critical, largely unexplored issue impacting the effectiveness of bulk MXene films. Traditionally, the degradation of MXenes in aqueous colloidal solutions has been attributed to oxidation reactions, mainly involving dissolved oxygen molecules, with water typically considered solely as a solvent.[25,26]

S. Huang et al.[27] showed that MXene hydrolysis, rather than oxidation with O_2, serves as the primary catalyst for MXene degradation. This revelation remains significant even in scenarios with minimal water exposure on the MXene surface. In a separate study by A. Lipatov et al.[28] investigated the environmental stability of individual defect-free MXene flakes obtained via a selective etching method. They demonstrated through electrical measurements that MXene flakes retained good conductivity after 24 h in humid air environments. Moreover, multilayer $Ti_3C_2T_x$ films displayed resistivity only one order of magnitude higher than individual flakes, showcasing the potential of MXene bulk films for EMI shielding applications.

The presence of intercalants within MXene film layers, such as Li^+, dimethyl sulfoxide (DMSO), and tetraalkylammonium hydroxides (TAAH) from the exfoliation process, has been identified as a primary factor contributing to poor hydration stability. H. Chen and co-workers[29] proposed an acid treatment method using ≈0.1 M HCl to efficiently remove Li^+ ions, common byproducts from the referred to as the clay method (mild etching or in-situ HF), the widely used route for obtaining well-delaminated MXene flakes. Films processed using this proton-acid treatment exhibited improved stability and EMI shielding performance compared to pristine films in humid air.

Environmental conditions aside, the choice of etching method significantly impacts the stability of the resulting MXene material. Aggressive procedures involving hydrofluoric acid can enhance the generation of defects, such as titanium vacancies on the MXene layer surface,[30] which can serve as active sites for the nucleation and growth of TiO_2.[31]

The parameter of SE correlates closely with the conductivity. Therefore, researchers have investigated changes in conductivity or resistivity over time as indicators of material stability.[32,33] Similarly, SE determination can serve as an indicator of material degradation, as is the particular case with $Ti_3C_2T_x$ films in harsh environments.[34]

In this study, two distinct $Ti_3C_2T_x$ materials were synthesized using a modified clay method[28] that included additional steps to enhance both the process yield and SE. Subsequently, a portion of the synthesized material, free from acid residues, underwent hand-shaking delamination for 5 min, while another portion underwent sonication for 10 min. SE measurements were conducted across a broad frequency range (1.5 to 10 GHz) using a coaxial probe derived from the standard D493518,[3,15,35] over a 28-day period to evaluate how environmental conditions affected the shielding performance of the $Ti_3C_2T_x$ material. These measurements served as an indicator of potential material degradation.

2. Results and Discussion

2.1. Synthesis and Characterization of MXene Films

This study is grounded in a modified procedure derived from the widely used clay method, enabling the production of monolayer MXene flakes with remarkable air stability and conductive properties.[13] In this modified process,[11] the etching step utilizes a higher molar ratio of LiF to the MAX-phase compared to the clay method, resulting in a higher quantity of intercalated Li^+ ions. These ions facilitate the exfoliation process by hydration, optimizing the aluminum etching process through a doubled HCl/LiF ratio (2:1). This results in well-exfoliated MXene flakes with a high surface area and defect-free characteristics, achieved without sonication. This etching method, followed by hand shaking for delamination is referred to in this work as MX-HS. However, the observed yield is notably low (≈4% wt.), which presents a significant limitation in the production of bulk MXene materials. To address this limitation, an additional sonication step for 10 min was introduced to enhance the yield of this synthesis procedure. Larger and defect-free flakes are essential for achieving optimal conductivity, a crucial factor for obtaining materials with excellent SE. Following sonication, the material was separated via centrifugation, discarding the smaller upper fraction above 3 500 rpm. Subsequently, the supernatant fraction within the range of 1500–3500 rpm was collected and utilized to fabricate MXene films. The obtained material is named as MX-US.

The conductivity and SE of both samples were measured to understand how the introduced modifications in relation to the original process influence the resulting material properties. In this study, films with a thickness of ≈4 µm were prepared using the two synthesized materials. Surprisingly, after both materials were stabilized for 48 h at room temperature with a 35%

of relative humidity (RH), MX-US exhibited a superior conductivity (3964.98 ± 46.54 S cm^{-1}) compared to MX-HS (1022.76 ± 3.12 S cm^{-1}). Additionally, the recorded EMI SE followed a similar trend, achieving a value of 56.09 ± 1.60 dB for MX-US and 41.26 ± 3.29 dB for MX-HS. Various parameters from the synthesis method employed, such as flake size, delamination level achieved, intercalants, oxidation degree, or the number of defects present on the MXene surface, are known to notably affect the electronic properties of the final MXene material produced. In the case of bulk materials such as MXene films, additional variables should be considered. Therefore, the technique used to obtain the film or its thickness will probably produce materials with different conductivity or EMI SE, even if the original MXene used to obtain the film came from the same synthesis method. Consequently, comparing the performance of MXene materials from different synthetic procedures or presented in different ways becomes challenging.

MXene is typically produced by the HF method or by the in situ HF (clay method) production. HF methods employ aggressive conditions of synthesis, along with an additional intercalation step followed by intensive sonication, which usually results in multilayer and defective materials with low conductivity values.[36–38] On the other hand, the clay method offers a less invasive approach suitable for producing well-delaminated MXene materials. In this case, the use of additional intercalants is unnecessary, since the Li^+ ions provided by the LiF used in the synthesis process suffice for this purpose. However, an intensive sonication step is usually required, and the eventual generation of defects can worsen their electrical conductivity.[28] Derived from the clay method, the MILD method can effectively delaminate MXene materials without any sonication step or additional intercalants, resulting in materials with excellent electronic features.[28,38–41] The MX-US synthesized material presents similarly outstanding electronic properties achieved by the MILD method and additionally improves greatly the yield of the process, which is crucial for producing MXene bulk materials.

The morphology of MX-US and MX-HS flakes was studied using field-emission scanning electron microscopy (FE-SEM), and the resulting micrographs are presented in **Figure 1**a,c, respectively.

While there is no notable difference in the size of the MXene flakes resulting from the synthesis method, the MX-HS material retained some unexfoliated particles that were absent in the other material. Moreover, the non-sonication method seems to produce a limited quantity of larger flakes alongside a considerable presence of smaller ones, resulting in a significant dispersion in the size of the obtained flakes.[23]

Transmission electron microscopy (TEM) images of MX-US and MX-HS are shown in Figure 1b and Figure 1d, respectively. The micrographs for both materials show single-layer flakes with defect-free surfaces and a similar size of ≈500 nm. Previous studies have suggested that integrating a non-sonication step into the synthesis process leads to larger single-layer flakes.[17,22] However, it is noteworthy that the dimensional characteristics of the original MAX-phase utilized could notably influence the final size of the etched material.[23]

Atomic force microscopy (AFM) was additionally employed to evaluate the effectiveness of the delamination achieved by both methods. The images obtained (**Figure 2**) led us to the same
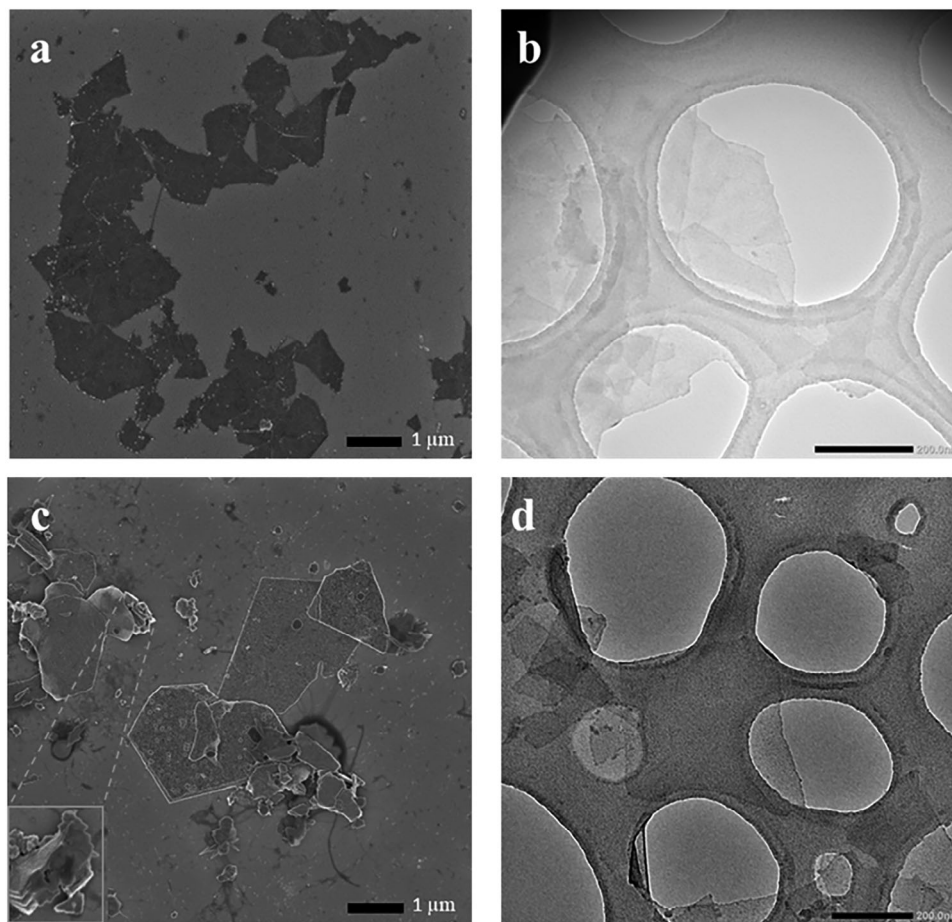
Figure 1. Morphology characterization of MXene flakes: a) FE-SEM image of MX-US; b) TEM micrograph of MX-US; c) FE-SEM image of MX-HS and d) TEM micrograph of MX-HS.
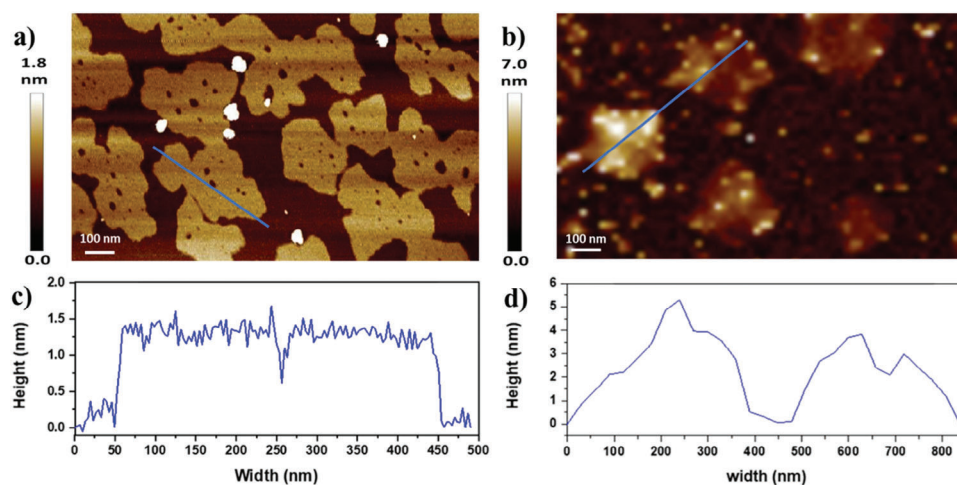

Figure 2. AFM images for a) MX-US and b) MX-HS. Height profiles obtained for c) MX-US and d) MX-HS.

conclusions regarding the morphology of MX-US and MX-HS as those achieved from SEM and TEM analysis. The flake size was similar in both cases, with no significant differences in their average size. However, the delamination degree was superior in MX-US compared to MX-HS, which exhibited some amount of stacked material. The excellent delamination observed for MX-US enabled the formation of more densely layered structures in their films, preventing oxidation and improving their conductivity and EMI shielding performance compared to MX-HS films.

AFM, SEM, and TEM analyses showed significant enhancement in the exfoliation process with the introduction of a brief and gentle sonication step. Additionally, the utilization of an intermediate ultracentrifugation fraction further amplified the yield without substantially altering the average sample size.

X-ray diffraction (XRD) serves as a useful tool for studying the structural characteristics of MXene-based material. The characteristic peaks attributed to Ti_3AlC_2 (Figure S1, Supporting Information) are not displayed in any MXene pattern (**Figure 2a**), confirming the adequacy of the applied etching procedure. However, in the MX-US material, only peaks associated with the (00l) reflections are present, indicating a highly ordered structure of stacked flakes. In contrast, MX-HS exhibits solely the peak corresponding to the (002) plane, suggesting a less ordered structure.

Additionally, the XRD spectrum showed a notable downshift between the (002) peaks of both materials, indicating a larger interlayer spacing in the MX-HS material (measuring 12.38 Å) compared to that of the MX-US (measuring 10.48 Å). This suggests that the presence of residual hydrated Li^+ ions[17] from the synthesis process could account for the larger interlayer distance.

The H_2O molecules associated with the lithium ions may contribute to the separation of the MXene layers, consequently leading to increased electrical resistance and a reduction in the SE properties of the material.[24]

The inclusion of the sonication step facilitated improved exfoliation and minimized the presence of synthesis by-products within the interlayer spacing. Consequently, this process resulted in a more efficient restacking, as observed in the diffraction pattern of MX-US, leading to a decrease in its electrical resistivity.[42,43]

Furthermore, the accommodation of H_2O molecules between the MXene layers[44] promotes the oxidation process and facilitates the formation of TiO_2 on the MXene surface. This phenomenon results in a swift decrease in the electronic conductivity of the sample.[29]

The chemical composition of the samples was further analyzed using both X-ray photoelectron spectroscopy (XPS) and ICP-MS techniques. The ICP-MS analysis revealed a distinct difference in the aluminum content between the samples. MX-US exhibited 0.78 wt% of aluminum, while the MX-HS sample showed a higher concentration of 2.69 wt%. This elevated aluminum content in MX-HS might be associated with an incomplete etching process, despite the absence of any MAX-phase peak in the XRD pattern. Another plausible explanation could be the presence of residual aluminum in the form of AlF_3 by-products on the surface of the stacked MXene layers.[45] The XPS results substantiate this assumption, indicating a 0.44 wt% aluminum content for MX-US and a significantly higher value of 12.21 wt% for MX-HS. The low aluminum content observed in the MX-US sample through XPS aligns consistently with the ICP-MS findings. How-

ever, the substantial increase in aluminum content detected in MX-HS by XPS suggests that most of the aluminum detected is situated on the surface rather than binding internally with the MXene layers. The significant presence of non-metallic aluminum on the surface of MX-HS material is likely to contribute to an increase in resistivity.[46]

Figure 3b,c displays the Ti2p spectra for MX-US and MX-HS, respectively. The XPS spectra for both materials exhibit doublets corresponding to the (Ti2p3/2 / Ti2p1/2) transitions.[22,30] These doublets indicate titanium interactions with carbons and terminal atoms, presenting Ti-C (454.56 / 460.52) eV and Ti−X from substoichiometric TiC_x (x < 1) or titanium oxycarbides (455.79 / 461.87) eV, respectively, in both materials. However, the specific doublet characteristic of the TiO_2 compound, associated with the sample oxidation, is exclusively observed in the MX-HS spectra (459.68 / 465.45) eV.[30–32] This confirms a higher degree of oxidation in the MX-HS compared to the MX-US sample.

Moreover, the O1s spectrum shown in Figure S2 (Supporting Information) provides further insights. The deconvolution of this signal in the MX-HS sample (Figure S2b, Supporting Information) reveals an additional peak at 534.11 eV, attributed to the presence of adsorbed water within the interlayer spacing of the MXene.[17,47] This finding corroborates the results obtained from the XRD measurements, which indicated a greater separation between the stacked layers in the MX-HS compared to the MX-US material. The detection of TiO_2 on the surface of MX-HS stands as another significant factor contributing to its lower conductivity and EMI SE compared to the MX-US material.[34]

Conductivity likely plays a significant role in the EMI shielding performance of MXene-based materials. Films synthesized from MX-US and MX-HS exhibited considerably different conductivity values, leading to different EMI SE. The characterization presented previously explained that the underlying reason for this unexpected difference between both materials stems from their different delamination degree. Although both MX-US and MX-HS showed similar average flake size, MX-HS achieved a lesser degree of delamination, resulting in a significant amount of stacked layers. The inter-flake spacing calculated from DRX patterns (Figure 3a) was larger for MX-HS than that of MX-US, indicating the presence of intercalants such as Li^+ and H_2O contributing to this enlarged interlayer spacing. Moreover, the presence of water among the layers facilitated the oxidation kinetics of Ti to TiO_2 (Figure 3), thereby reducing the conductivity of MXene.

$Ti_3C_2T_x$ is essentially a metallic-like conductor,[48,49] and its conductive behavior can be explained by a conductive term due to intra-flake resistance and an insulating term due to inter-flake resistance acting in series.[50] Assuming that intra-flake metallic conductivity is described by the Drude equation and mainly affected by the charge carriers' density, the superior oxidation degree of the MX-HS, triggered by the intercalated water molecules, significantly reduced the conductive term of this sample. Water molecules adsorbed onto the MXene surface can also act as electron acceptors.[28,51] Since electrons are the main charge carriers present in MXene materials, the conductivity of the sample will be reduced by the presence of these adsorbates. Additionally, the different conductivity behavior of MX-HS compared to MX-US must also be influenced by the presence of intercalants, which increased the interlayer spacing in the stacked MXene
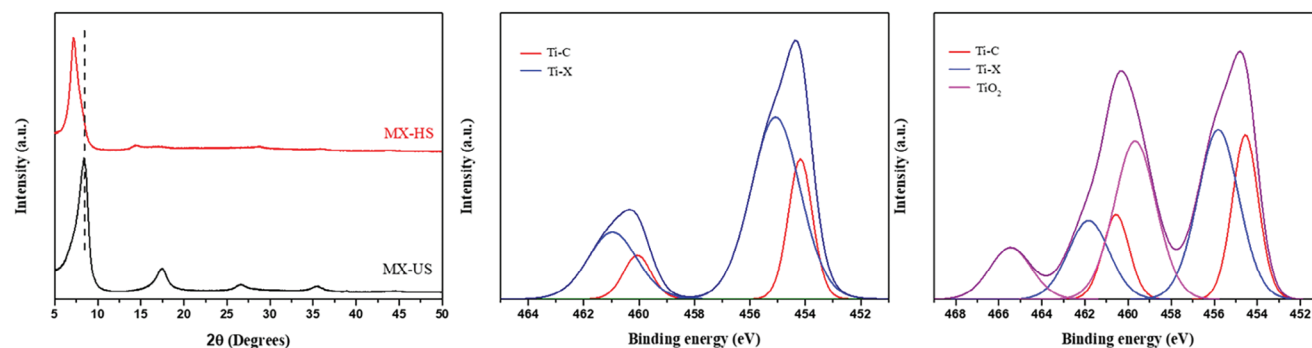
**ADVANCED
SCIENCE NEWS**

www.advancedsciencenews.com

**ADVANCED
ELECTRONIC
MATERIALS**

www.advelectronicmat.de

Figure 3. a) XRD diffraction patterns of MX-US and MX-HS. b) Ti2p region XPS spectra of MX-US and c) Ti2p region XPS spectra of MX-HS.

sheets. Consequently, the larger interlayer spacing, the greater the resistance,[44,52–56] and the more representative the insulating term describing the electrical behavior of the samples. In summary, both oxidation and intercalation contributed to introducing remarkable differences in the conductivity and EMI SE of both samples, underscoring the importance of intercalants, particularly intercalated water molecules, in determining the final electrical properties of MXene materials.

2.2. Stability Study of MXene Film in Humid Environment

The oxidation process leading to the formation of TiO_2 on the surface of MXenes, significantly reduces their electrical conductivity and, consequently, their effectiveness in electromagnetic shielding. Integrating MXenes into continuous layers on various materials is a promising industrial approach for utilizing MXenes as EMI shielding materials. Despite this, few studies have assessed how environmental conditions affect the SE properties of these materials. MXene-based materials have been observed to oxidize more rapidly in the presence of water, progressing swiftly in aqueous dispersions of MXene[26] or high-humidity environments.[29] Therefore, evaluating the impact of humidity levels on the degradation process of MXenes is crucial for understanding the behavior of these innovative materials.

Given that MX-US demonstrated superior EMI SE compared to MX-HS, it was chosen to fabricate the MXene films for this study. Films with an approximate thickness of 4 μm were subjected to two controlled RH environments at room temperature for a month. One sample, labeled MX-US-35 (**Figure 4a,c**) was placed in a 35% RH environment, while another, named MX-US-70, was exposed to a 70% RH environment. The impact of varying degradation levels on both conductivity and SE was assessed, using these measured parameters to evaluate the oxidation degree of the material.

The changes in both samples after being placed in different humid environments for a month were studied using TEM. It has been reported that the oxidation of MXene generates TiO_2, detectable on its surface through TEM images.[26] From Figure 4b,d, micrographs recorded for both samples showed clean and clear flakes without any evidence of dark points on their surfaces or edges, indicative of the presence of titanium dioxide.[57] However, more irregular edges were observed for the MX-US-70 sample (Figure 1b), indicating a higher degree of degradation

compared to MX-US-35 (Figure 1d). This highlights the influence of RH on the degradation process of the flakes, which occurs more rapidly as the presence of water in the environment increases.

X-ray Diffraction (XRD) was used to detect structural alterations in MXene films, as illustrated in **Figure 5**, displaying the evolution of the samples' diffraction patterns. The peak associated with the (002) plane reflects the arrangement in the basal direction of the characteristic lamellar stacked structure of MXene materials.[32] In this context, oxidation progresses through the diffusion of water molecules and oxygen among the MXene layers, leading to titanium dioxide formation on the MXene surface and an expansion of the interlayer spacing. Consequently, a shift of the (002) peak signal toward lower angles signifies the disruption of the lamellar structure, indicating the degradation of the MXene. As seen in Figure 5a, the (002) peak for MX-US-35 has shifted from its original position, with the interlayer d-spacing increasing from 10.60 Å to 11.18 Å. Similarly, albeit with a more pronounced change in the interlayer spacing, the pattern for MX-US-70 exhibits an increase from 12.86 Å to 14.24 Å, indicating a higher degree of oxidation. Additionally, upon closer inspection of Figure 5b, a broad band centered ≈25 degrees suggests the formation of TiO_2 on the MXene surface.[58] The evolution of interlayer spacing over time is depicted in Figure 5c, showing a consistent linear behavior for both studied humidity conditions. However, the slope observed for MX-US-70 is more pronounced than that of MX-US-35, suggesting that higher RH leads to faster degradation of the layered structure for MX-US-70. The strong dependency of conductivity on inter-layer spacing, as shown in Figure 5d, indicates that the conduction process in these samples is likely more dependent on inter-flake electron hopping transport across the MXene layers than on intra-flake conduction processes.[52]

The electrical conductivity and electromagnetic SE of both MX-US-35 and MX-US-70 were measured at seven-day intervals over a month, and the results are depicted in **Figure 6** and Figure 8, respectively. Initial values for both samples were obtained after allowing the materials to stabilize for 48 h in their respective humidity environments. These parameters are closely interrelated, serving as indicators of oxidation extent in MXene-based materials. As previously mentioned, material degradation due to TiO_2 formation on the MXene surface compromises its conductivity properties, resulting in an expected decrease in the EMI shielding values.[59]

2400024 (6 of 12)

**ADVANCED
SCIENCE NEWS**

www.advancedsciencenews.com

**ADVANCED
ELECTRONIC
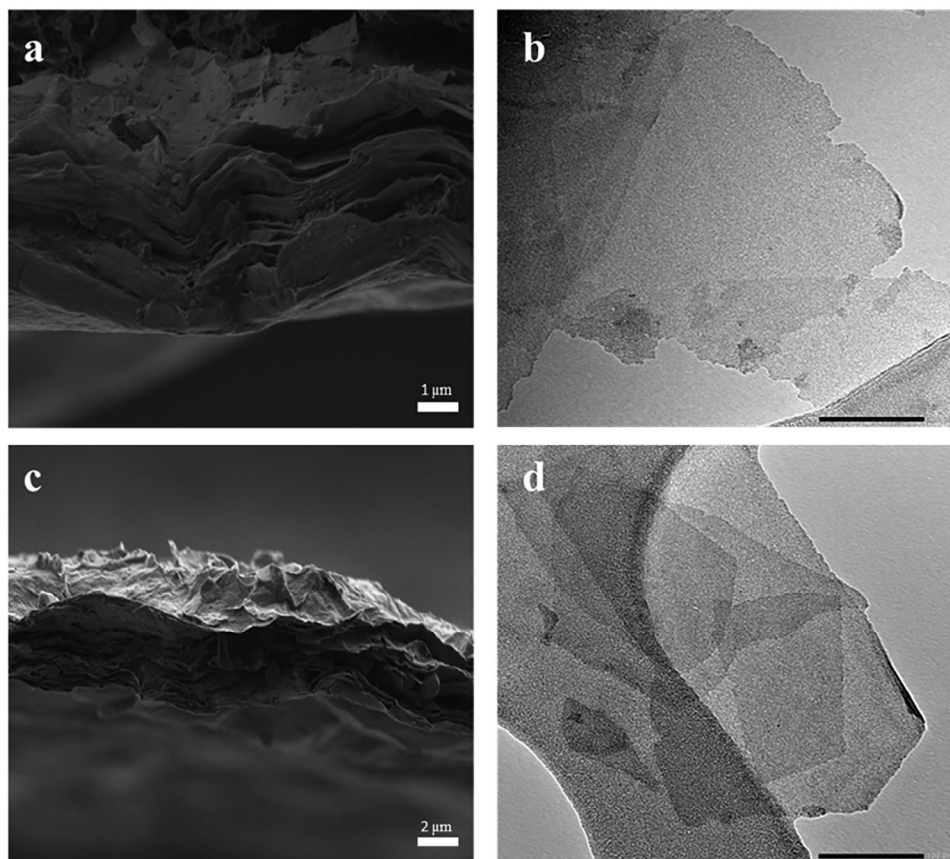MATERIALS**

www.advelectronicmat.de

Figure 4. Sections (a) and (c) display SEM images at different magnifications of the film obtained from the MX-US process using the vacuum-assisted filtration method. Sections (b) and (d) show flakes from MX-US-70 and MX-US-35 observed by TEM after a 28-day stability test, respectively.

The trend in film conductivity values shown in Figure 6 demonstrates the evident impact of exposure to different RH environments on sample electrical performance. At 35% RH, the observed value after 14 days of testing was 97.28% of the initial value, indicating negligible degradation during this period. After the full four-week test, the MX-US-35 sample exhibited a conductivity value of 3571.72 ± 16.66 S cm^{-1}, representing 89.88% of the initial value of 3973.72 ± 121.3 S cm^{-1}. Additionally, the sample was measured after 6 months of exposure (180 days) with a moderate reduction in its conductivity. Conversely, the MX-US-70 sample showed a more pronounced loss of conductivity. During the first week, the sample experienced a decrease of 43.44% from its initial value of 2531.34 ± 13.46 S cm^{-1}, and after 14 days, it retained only 23.26% of the initial value. By the end of the four-week period, it retained 17.07% of its initially measured conductivity.

The noticeable disparity in oxidation degrees between the samples can be attributed to their exposure to different RH environments. Previous studies have reported the rapid degradation of MXene flakes either in humid ambient or aqueous dispersions.[26,60,61] In these conditions, water plays a pivotal role in the oxidation process of MXene flakes, with hydrolysis being the primary cause leading to the transformation of Ti into titanium dioxide.[27] The kinetics of Ti3C2Tx degradation have been studied previously using UV-vis transmittance spectroscopy,[26,62,63] with the data fitted to the exponential decay function:

$$A = A_i e^{-t/\tau} \tag{1}$$

where τ represents the time constant of the oxidation process. Notably, S. Huang and V-N Mochalin[27] found that the time constant for $Ti_3C_2T_x$ dispersed in isopropanol/O$_2$ medium was 436.53 times higher than that of the same MXene material dispersed in water/O$_2$ medium, indicating that water significantly accelerates the degradation of $Ti_3C_2T_x$ compared to oxygen. Therefore, it is expected that the higher humidity levels will result in increased oxidation. Molecular dynamic simulations at room temperature conducted by T. Wu et al.[64] aimed to elucidate how water interacts with MXene. They observed the irreversible adsorption of water molecules onto Ti atoms, leading to the cleavage of Ti-C bonds and promoting the MXene hydrolysis at room temperature. Furthermore, the simulations showed that an increase in the amount of intercalated water molecules accelerated the oxidation kinetics. These findings are consistent with the increase in the oxidation degree observed in our samples with higher ambient humidity. On the other hand, it is understood that the nucleation and growth of TiO$_2$ on the MXene layers involve the diffusion of both electrons and titanium ions. Hence, the presence of an appropriate solvent such as water
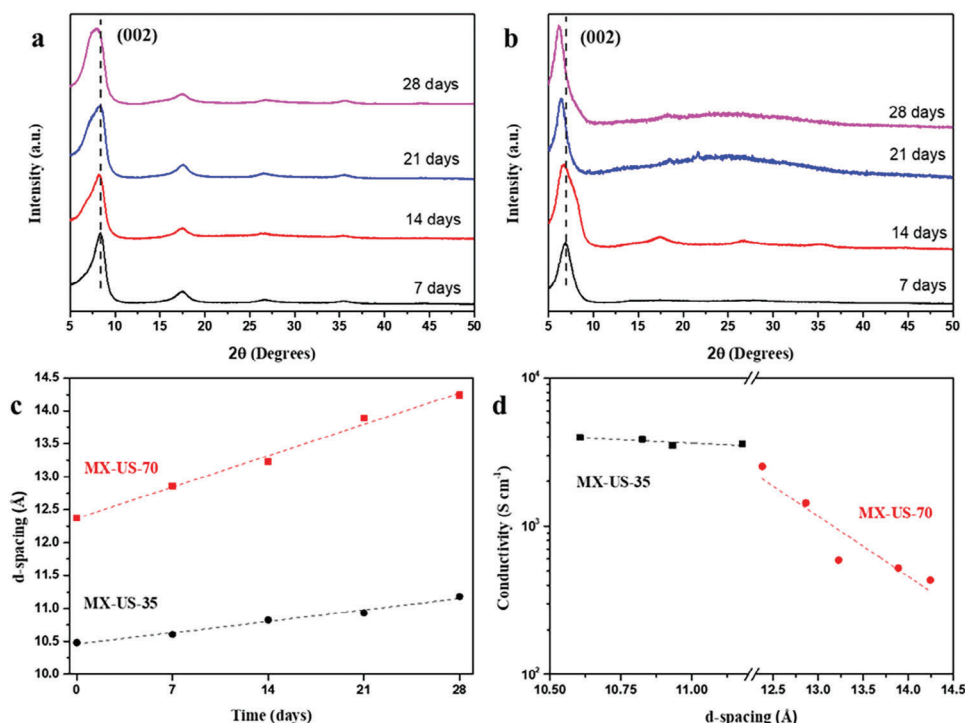
Figure 5. Evolution of XRD diffraction spectra throughout the 28-days stability test for a) MX-US-35 and b) MX-US-70, c) shows the increase in d-spacing over time for MX-US under both environmental conditions studied, d) depicts the conductivity versus d-spacing for both samples.

facilitates the transport of O^{2-} and Ti^{4+} ions, enhancing the efficacy of the oxidation reaction.[31]

Therefore, the lower conductivity values observed for MX-US-70 can be attributed to the higher RH environment in which it was placed. This condition increased the presence of water molecules within the MXene interlayer spacing and, on its surface, facilitated the formation of TiO_2. Consequently, this resulted in a more significant reduction in its conductivity.

2.3. SE Characterization

The study employed a test method based on the measurement technique outlined in the ASTM D4935-18 standard.[3] This standard defines a procedure for measuring the electromagnetic SE of planar materials against plane, far-field EM waves. To conduct SE measurements of MXene samples beyond the maximum frequency limit stated in the aforementioned standard, a smaller
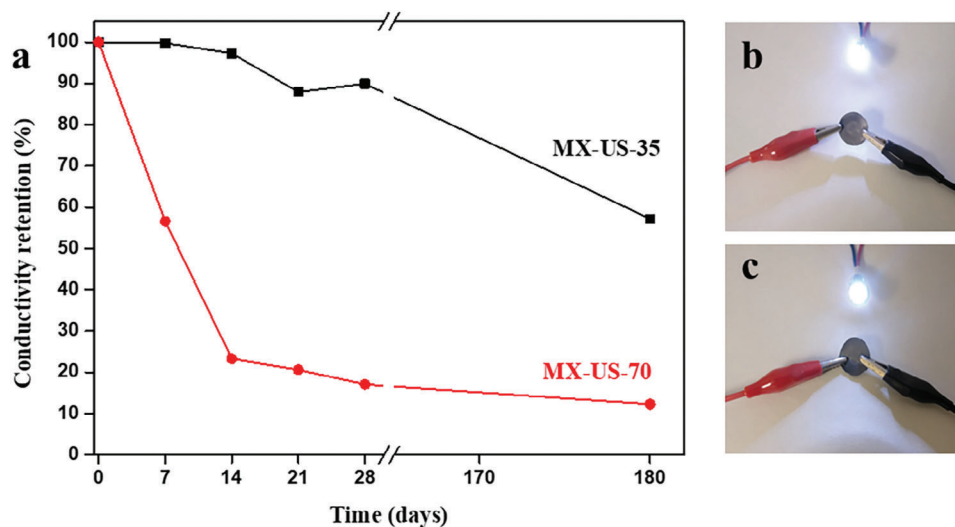

Figure 6. a) Illustrates the conductivity retention capacity over time for both MX-US samples under different environmental conditions. b) and c) depict the MX-US-70 and MX-US-35 membranes after a 180-days test under the selected controlled humidity conditions.
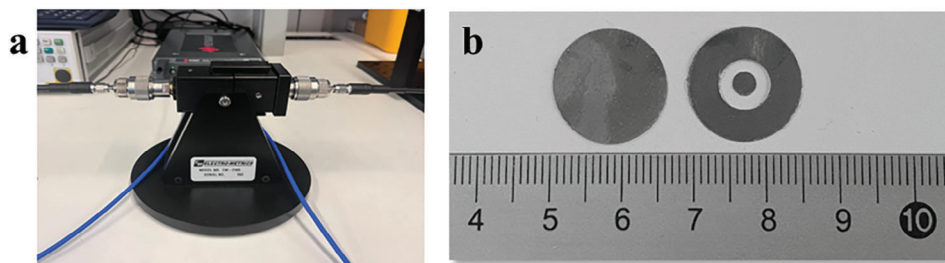
**ADVANCED
SCIENCE NEWS**

www.advancedsciencenews.com

**ADVANCED
ELECTRONIC
MATERIALS**

www.advelectronicmat.de

Figure 7. (a) shows the experimental measurement setup derived from the ASTM D4935 standard. (b) represents an example of the geometry and dimensions of the measured samples.

coaxial cell holder was employed (as shown in **Figure 7a**). The measurement setup requires test samples with specific geometry and small dimensions. An example of such test samples used in this study is depicted in Figure 7b.

The SE of the samples was assessed under the same conditions used for conductivity measurements. The results, depicted in **Figure 8a**, revealed a parallel trend between the EMI SE values and the electrical conductivity. After a 28-days period, MX-US-35 retained 93.26% of its initial value of 56.09 ± 1.60 dB. The value obtained at the 180-day test was 51.44 ± 1.87 dB, representing 91.71% of its initial value. In contrast, MX-US-70 maintained 74.36% of its initial value of 48.77 ± 0.77 dB at the 28-day test and 71.25% at the 180-day test under controlled humidity conditions. The slight divergence observed in the initial values for both samples might be attributed to their exposure period of 48 h in environments with 35% and 70% humidity for MX-US-35 and MX-US-70, respectively.

The considerable impact of water adsorption on MX-US-70 significantly affected its conductivity and, consequently, its SE performance.[65] The decline in shielding capacity for MX-US-70 does not demonstrate a direct correlation with the conductivity loss observed in this sample, as noted in the case of MX-US-35. This inconsistency could be attributed to the various mechanisms influencing EMI shielding. Although MXene materials primarily exhibit reflection losses due to conductivity,[22] they can also display losses associated with dipolar polarization from surface functional groups or localized defects, as well as electromagnetic radiation absorption between material layers.[66]

These aspects may not be as significantly affected by oxidation as the reflection losses. Therefore, the reduction observed in the

material's SE is not as substantial as the decrease in its conductivity, indicating that using conductivity measurements to evaluate degradation and extrapolate EMI SE values might not accurately portray the performance of MXene materials. The EMI shielding results for both samples exposed to different RH environments validate the impact of water in the degradation of MXene-based films.

Figure 8b illustrates the SE provided by the MX-US-35 and MX-US-70. The SE of the samples is depicted under initial humidity conditions, as well as after exposure to controlled humidity conditions for 28-day (Figure 8b) and a 180-day test period. The results exhibited a significant decrease in the SE of the MX-US-70, by ≈ 7.32 dB, across the entire studied frequency range after a 48-h exposure to controlled humidity environments. These findings demonstrate that even a brief exposure of 48 h to high humidity can notably impact the SE of the samples.

Regarding the evolution of the SE parameter concerning exposure time to a humid environment, it is evident that the MX-US-35 sample experiences a reduction of 4.95 dB after a 28-day test and 4.65 dB at the 180-day test period, showing the outstanding stability of the sample placed at 35% RH conditions. However, the MX-US-70 sample undergoes a more notable reduction, considering its mean SE of 48.77 ± 0.77 dB under initial conditions, whereas, after exposure to 70% RH for 28-day period, the mean SE dropped by ≈ 12.51 dB, and for the extended 180-day test, it displayed a decrease of 14.02 dB. Consequently, the analysis of the SE parameter concerning frequency follows the trend observed in conductivity results. It is essential to note that the SE performance of MXene samples is remarkable, providing a consistent and uniform shielding response across the entire
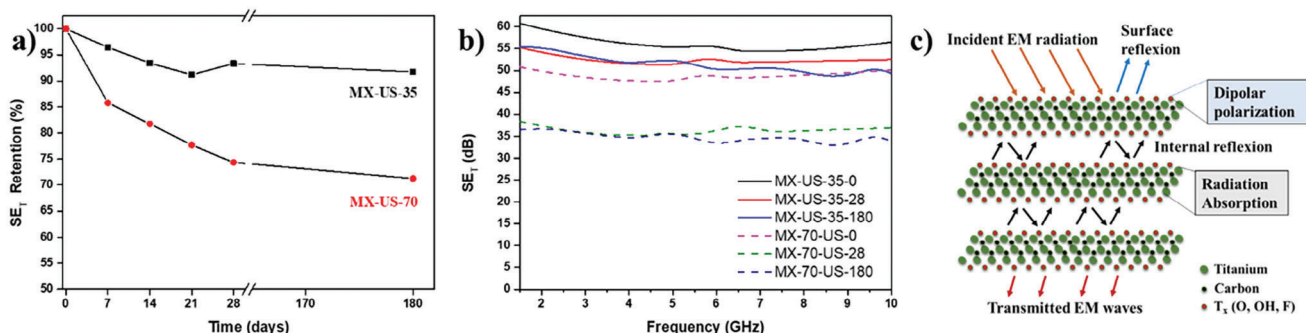

Figure 8. (a) depicts the retention capacity of EMI SE for both samples. (b) illustrates the EMI SE performance from 1.5 to 10 GHz for MX-US-35 and MX-US-70 results after keeping the samples for 0, 28, and 180 days in controlled humidity test conditions. (c) represents the EMI shielding mechanism suggested for $Ti_3C_2T_x$ material.

2400024 (9 of 12)

**ADVANCED
SCIENCE NEWS**

www.advancedsciencenews.com

**ADVANCED
ELECTRONIC
MATERIALS**

www.advelectronicmat.de

frequency range studied. Moreover, the SE value of MXene material is notably higher when compared to other alternative shielding materials, particularly considering that the thickness of the analyzed MXene samples is ≈4 μm.[4,67,68]

The exceptional performance of the studied MXene films as EMI shielding materials can be explained by the mechanism illustrated in Figure 8c. Initially, incident electromagnetic radiation undergoes attenuation through reflection, owing to the high surface conductivity of the $Ti_3C_2T_X$, resulting from the abundance of free charge carriers present on their surface.[69] These carriers are responsible for reflecting the incoming EM waves upon reaching the surface. The portion of the EM radiation that is not reflected on the MXene surface penetrates the densely charged conductive layer, interacting with the waves and reducing their energy through effective absorption.[22,70] Additionally, the pores present in the MXene flakes create impedance mismatch regions with internal interfaces, promoting a multiple reflection process and increasing the absorption of the remaining waves.[68] Additionally, the layered structure of the re-stacked MXene flakes facilitates successive internal reflections, aiding in the absorption of electromagnetic waves that are not initially reflected by the surface or absorbed through the MXene layer, subsequently dissipating them as heat.[70,71] This process iterates as the remaining EM waves reach subsequent layers. Furthermore, the surface terminations located on the MXene surface, primarily Ti-O and Ti-F bonds, contribute to the material's EMI shielding capacity by inducing polarization losses when interacting with an electromagnetic alternating field.[22]

3. Conclusion

In summary, our study presents a novel protocol for selectively etching aluminum from Ti_3AlC_2, resulting in a substantial increase in the yield of MXene flakes compared to conventional non-sonication minimally invasive methods. This approach effectively addresses the challenges associated with sonication steps by offering precise control over the size of the flakes.

The films derived from the flakes synthesized through this novel protocol exhibited significantly enhanced conductivity and EMI SE compared to those prepared using the traditional MILD method. This improvement underscores the potential of our synthesis protocol in optimizing crucial MXene material properties for EMI shielding applications. Furthermore, the shielding effectiveness (SE) results demonstrated the remarkable ability of MXene samples to deliver a consistent flat response across the entire frequency region (FR) studied, covering the main part of the FR1 employed by 5G communications. Notably, the SE values of MXene material surpassed those of alternative shielding materials, including composites based on CNTs, highlighting their efficacy despite the relative thin thickness of the analyzed MXene samples (≈4 μm).

The additional characterization of the conductivity and SE of the MXene films provided invaluable insights into material degradation in humid environments. The synthesized MXene films exhibited exceptional oxidation stability at 35% RH, retaining 93.26% of their initial SE value after the 28-day test and 91.71% after the 180-day test in a controlled humidity environment representative of typical indoor conditions. Measurements conducted at 70% RH underscored the significant influence of water over oxygen in the degradation process of MXene materials.

Ultimately, our employed novel synthesis protocol has demonstrated its efficacy in producing $Ti_3C_2T_x$ with markedly improved synthesis yield and outstanding properties suitable for application as bulk EMI shielding material. This work not only advances MXene synthesis methodologies but also highlights their potential in providing reliable and stable EMI shielding solutions, offering promising avenues for future industrial applications.

4. Experimental Section

MXene Synthesis: $Ti_3C_2T_x$ was synthesized through the selective etching of Al from Ti_3AlC_2 MAX phase (obtained from Carbon Ukraine, Ltd.) using a LiF/HCl solution following a modified method described by Lypatov et al.[28] Typically, 1 g of LiF (Sigma-Aldrich) was added to 20 mL of 6 M HCl solution (Sigma-Aldrich) and stirred until a clear solution was observed. Subsequently, 1 g of Ti_3AlC_2 powder was slowly introduced into this solution, and the mixture was stirred using a magnetic polytetrafluoroethylene stirrer at 35 °C for 24 h. The resulting suspension was centrifuged at 3 500 rpm, and the supernatant fraction was discarded. The black sediment settled at the bottom of the flask underwent multiple washes with distilled water purged with Argon until the pH of the supernatant reached ≈6. Following this, the deposited MXene material was dispersed in water and delaminated either by hand shaking for 5 min (MX-HS) or through bath sonication at room temperature for 10 min (MX-US), followed by centrifugation at 3 500 rpm for 1 h. Subsequently, the colloidal supernatant aqueous dispersion of delaminated MXene obtained for MX-HS was collected and dried by lyophilization. For MX-US, aimed at increasing the flakes size, the supernatant fraction obtained after centrifugation at 3 500 rpm for 1 h was discarded. Another centrifugation step at 1 500 rpm for 1 h was performed, and the resulting supernatant fraction was collected and dried by lyophilization to obtain the MX-US material.

Preparation of MXene Films: MXene films were fabricated using the vacuum-assisted filtration method (VAF) employing nylon membranes with a pore size of 0.22 μm. Diluted aqueous dispersions of MX-US (1 mg mL⁻¹) were used to produce films with an approximate thickness of ≈4 μm. Subsequently, the films were vacuum-dried overnight at room temperature and stored in a desiccator.

X-Ray Diffraction Analysis: XRD patterns of the MXene based materials were recorded on a Brucker D2 phaser instrument, with Cu K radiation (λ = 1.5406 Å) and a step size of 0.02 min⁻¹, in the 2θ range between 5 and 65.

X-Ray Photoelectron Spectroscopy (XPS): XPS technique was used to study the chemical composition of the samples. XPS spectra of MXene samples were acquired by means of Thermo Fisher Scientific VG-Microtech Multilab 3000 photoelectron spectrometer.

Morphological Analysis: Solutions from both samples were drop-cast onto silicon substrates, and images were acquired using a Field Emission Scanning Electron Microscope (FESEM), Zeiss Ultra 55 instrument. Transmission Electron Microscopy (TEM) images of the MXene flakes were obtained using the JEM-1010 (JEOL DEBEN AMT, Tokyo, Japan). Atomic Force Microscopy (AFM) images were recorded in a tapping mode using a Bruker-Multimode instrument. The analysis of the obtained results was made by Nanoscope 1.8 Analysis software.

Conductivity Measurement: The sheet resistance of the prepared MXene films was measured using a four-point probe system (Ossila Ltd., Sheffield UK). The resulting conductivity was calculated using Equation 1.

$$\sigma = \frac{1}{R_s t} \qquad (2)$$

where σ is the electrical conductivity (S cm⁻¹), R_s denotes the sheet resistance (Ω sq⁻¹) and t is the thickness of the film (cm).

**ADVANCED
SCIENCE NEWS**

www.advancedsciencenews.com

**ADVANCED
ELECTRONIC
MATERIALS**

www.advelectronicmat.de

SE measurement: This study involved assessing the SE following the ASTM D4935 standard. However, a crucial limitation of the ASTM D4935-18 standard should be highlighted. Specifically, the maximum frequency operation of the test system is limited to 1.5 GHz. This limitation constrains the upper bound of the testing range. The frequency range limits of ASTM D4935-18 standard are determined by decreased displacement current at lower frequencies and the activation of modes other than the transverse electromagnetic mode (TEM) at higher frequencies due to the size of the coaxial sample holder. This method is suitable for measuring the SE of planar materials under normal incidence, far-field, and plane-wave conditions, considering E and H tangential to the material surface.

The procedure involves the evaluation of insertion loss (IL) by introducing test samples into a coaxial two-conductor transmission line holder supporting TEM propagation mode. The ASTM D4935-18 probe comprises a two-port flanged coaxial sample holder with a characteristic impedance of 50 Ω, utilizing an Electro-Metrics commercial probe model EM-2108. Coaxial cables connect the two halves of the CSH to a vector network analyzer (VNA) with two ports, specifically the VNA P9375A Keysight Streamline USB,[72] enabling tests from 300 KHz up to 26.5 GHz with a dynamic range between 85 dB and 95 dB (frequency-dependent). To perform the test, two specimens of identical material and thickness are required: the reference and the load. The load specimen should be disk-shaped with a diameter matching that of the outer CSH flange. Conversely, the reference specimen should comprise two components: a washer, and a disk-shaped sample matching the dimensions of the outer and inner conductors, respectively. The utilization of these different specimens is warranted as the reference specimen can partially compensate for capacitive coupling effects by establishing a frequency-dependent reference level.[73] The SE is determined by assessing the difference between the load measurements and those of the reference specimen. This difference is caused by the reflection and absorption of the material between the two flanges of the coaxial cell. SE is expressed in decibels as is described in Equation 2:

$$SE = 20\log_{10}\left|\frac{S_{21,R}}{S_{21,L}}\right| \tag{3}$$

where $S_{21,R}$ and $S_{S21,L}$ represent the measured transmission scattering parameters of the reference and load specimen, respectively.

Supporting Information

Supporting Information is available from the Wiley Online Library or from the author.

Acknowledgements

Conflict of Interest

The authors declare no conflict of interest.

Data Availability Statement

The data that support the findings of this study are openly available in RiuNet at https://riunet.upv.es/, reference number 1.

Keywords

[1] J. Victoria, A. Suarez, P. A. Martinez, A. Alcarria, A. Gerfer, J. Torres, *IEEE Trans. Electromagn. Compat.* **2020**, *62*, 1504.

[2] P. A. Martinez, E. A. Navarro, J. Victoria, A. Suarez, J. Torres, A. Alcarria, J. Perez, A. Amaro, A. Menendez, J. Soret, *Electronics* **2021**, *10*, 2201.

[3] Standard Test Method for Measuring the Electromagnetic Shielding Effectiveness of Planar Materials, https://doi.org/10.1520/D4935-18, (accessed: May 2018).

[4] A. Amaro, A. Suarez, A. Tamburrano, J. Torres, F. Marra, P. A. Martinez, B. Galindo, N. Soriano, J. Victoria, A. Alcarria, *IEEE Trans. Electromagn. Compat.* **2023**, *65*, 177.

[5] A. Tamburrano, D. Desideri, A. Maschio, M. S. Sarto, *IEEE Trans. Electromagn. Compat.* **2014**, *56*, 1386.

[6] M. S. Sarto, A. Tamburrano, *IEEE Trans. Electromagn. Compat.* **2006**, *48*, 331.

[7] J. M. Thomassin, C. Jérôme, T. Pardoen, C. Bailly, I. Huynen, C. Detrembleur, *Mater. Sci. Eng.: R: Rep.* **2013**, *74*, 211.

[8] E. F. Vance, W. Graf, *IEEE Trans. Electromagn. Compat.* **1988**, *30*, 294.

[9] I. R. Ibrahim, K. A. Matori, I. Ismail, *Sci. Rep.* **2020**, *10*, 3135.

[10] B. Zhao, B. Zhao, J. Deng, R. Zhang, L. Liang, B. Fan, Z. Bai, G. Shao, C. B. Park, *Eng. Sci.* **2018**, *3*, 5.

[11] J. Victoria, A. Suarez, J. Torres, P. A. Martinez, A. Alcarria, J. Martos, R. Garcia-Olcina, J. Soret, S. Muetsch, A. Gerfer, *Materials* **2018**, *11*, 1612.

[12] A. Iqbal, J. Kwon, M. K. Kim, C. M. Koo, *Mater. Today Adv.* **2021**, *9*, 100124.

[13] M. Qin, L. Zhang, H. Wu, *Adv. Sci.* **2022**, *9*, 2105553.

[14] A. Amaro, A. Suarez, J. Torres, P. A. Martinez, R. Herraiz, A. Alcarria, A. Benedito, R. Ruiz, P. Galvez, A. Penades, *Magnetochemistry* **2023**, *9*, 114.

[15] P. A. Martinez, J. Victoria, J. Torres, A. Suarez, A. Alcarria, A. Amaro, B. Galindo-Galiana, C. Losada-Fernandez, V. Ramirez-Monsell, B. Lopez-Rius, in 2021 IEEE International Joint EMC/SI/PI and EMC Europe Symposium, IEEE, **2021**, 278, https://doi.org/10.1109/EMC/SI/PI/EMCEurope52599.2021.9559349.

[16] D. D. L. Chung, *Carbon* **2001**, *39*, 279.

[17] Z. Wang, Z. Cheng, C. Fang, X. Hou, L. Xie, *Composites, Part A* **2020**, *136*, 105956.

[18] M. Han, C. E. Shuck, R. Rakhmanov, D. Parchment, B. Anasori, C. M. Koo, G. Friedman, Y. Gogotsi, *ACS Nano* **2020**, *14*, 5008.

[19] L. Wang, J. Cheng, Y. Zou, *Adv Compos Hybrid Mater* **2023**, *6*, 172.

[20] T. T. Liu, Y. H. Zhu, J. C. Shu, M. Zhang, M. S. Cao, *Mater. Today Phys.* **2023**, *31*, 100988.

[21] Q. Q. Wang, W. Q. Cao, M. S. Cao, *2D Mater.* **2024**, *11*, 012001.

[22] F. Shahzad, Science, https://www.science.org.

[23] W. T. Cao, F. F. Chen, Y. J. Zhu, Y. G. Zhang, Y. Y. Jiang, M. G. Ma, F. Chen, *ACS Nano* **2018**, *12*, 4583.

[24] S. Yang, P. Yang, C. Ren, X. Zhao, J. Zhang, *J. Colloid Interface Sci.* **2022**, *622*, 97.

[25] G. Deysher, S. Sin, Y. Gogotsi, B. Anasori, *Mater. Today* **2018**, *21*, 1064.

[26] C. J. Zhang, S. Pinilla, N. McEvoy, C. P. Cullen, B. Anasori, E. Long, S. H. Park, A. S. Ascaso, A. Shmeliov, D. Krishnan, C. Morant, X. Liu, G. S. Duesberg, Y. Gogotsi, V. Nicolosi, *Chem. Mater.* **2017**, *29*, 4848.

[27] S. Huang, V. N. Mochalin, *Inorg. Chem.* **2019**, *58*, 1958.

[28] A. Lipatov, M. Alhabeb, M. R. Lukatskaya, A. Boson, Y. Gogotsi, A. Sinitskii, *Adv. Electron. Mater.* **2016**, *2*, 1600255.

[29] H. Chen, Y. Wen, Y. Qi, Q. Zhao, L. Qu, C. Li, *Adv. Funct. Mater.* **2020**, *30*, 1906996.

**ADVANCED
SCIENCE NEWS**

www.advancedsciencenews.com

**ADVANCED
ELECTRONIC
MATERIALS**

www.advelectronicmat.de

[30] X. Sang, Y. Xie, M. W. Lin, M. Alhabeb, K. L. V. Aken, Y. Gogotsi, P. R. C. Kent, K. Xiao, R. Raymond, *ACS Nano* **2016**, *10*, 9193.

[31] F. Xia, F. Xia, J. Lao, R. Yu, X. Sang, J. Luo, Y. Li, J. Wu, *Nanoscale* **2019**, *11*, 23330.

[32] A. D. Dillon, M. J. Ghidiu, A. L. Krick, J. Griggs, S. J. May, Y. Gogotsi, M. W. Barsoum, A. T. Fafarman, *Adv. Funct. Mater.* **2016**, *26*, 4162.

[33] Y. Chae, S. J. Kim, S. Y. Cho, J. Choi, K. Maleski, B. J. Lee, H. T. Jung, Y. Gogotsi, Y. Lee, C. W. Ahn, *Nanoscale* **2019**, *11*, 8387.

[34] Y. Da, Q. Qu, L. Kong, Q. Liu, M. Zhu, Y. Du, X. Tian, Y. Liu, H. Wang, *RSC Adv.* **2023**, *13*, 6619.

[35] A. S. Zapata, J. F. Dawson, J. Ariën, J. Catrysse, D. Pissoort, A. C. Marvin, *IEEE Electromagn. Compat. Mag.* **2023**, *12*, 78.

[36] Z. Ling, C. Ren, M. Q. Zhao, J. Yang, J. M. Giammarco, J. Qiu, M. W. Barsoum, Y. Gogotsi, *Proc. Natl. Acad. Sci. U. S. A.* **2014**, *111*, 16676.

[37] M. Q. Zhao, C. E. Ren, Z. Ling, M. R. Lukatskaya, C. Zhang, K. L. V. Aken, M. W. Barsoum, Y. Gogotsi, *Adv. Mater.* **2015**, *27*, 339.

[38] M. Alhabeb, K. Maleski, B. Anasori, P. Lelyukh, L. Clark, S. Sin, Y. Gogots, *Chem. Mater.* **2017**, *29*, 7633.

[39] C. E. Shuck, M. Han, K. Maleski, K. Hantanasirisakul, S. J. Kim, J. Choi, W. E. B. Reil, Y. Gogotsi, *ACS Appl. Nano Mater.* **2019**, *2*, 3368.

[40] K. Maleski, C. E. Ren, M. Q. Zhao, B. Anasori, Y. Gogotsi, *ACS Appl. Mater. Interfaces* **2018**, *10*, 24491.

[41] J. Chen, J. Chen, B. Yang, Y. D. Lim, W. Duan, Y. Zhao, B. K. Tay, X. Yan, *Nanotechnology* **2020**, *31*, 285701.

[42] T. Zhang, T. Zhang, L. Chang, X. Zhang, H. Wan, N. Liu, L. Zhou, X. Xiao, *Nat. Commun.* **2022**, *13*, 6731.

[43] H. Wang, H. Wang, Y. Wu, J. Zhang, G. Li, H. Huang, X. Zhang, Q. Jiang, *Mater. Lett.* **2015**, *160*, 537.

[44] J. Halim, J. Halim, S. Kota, M. R. Lukatskaya, M. Naguib, M. Q. Zhao, E. J. Moon, J. Pitock, J. Nanda, S. J. May, Y. Gogotsi, M. W. Barsoum, *Adv. Funct. Mater.* **2016**, *26*, 3118.

[45] H. Shi, H. Shi, P. Zhang, Z. Liu, S. W. Park, M. R. Lohe, Y. Wu, A. S. Nia, S. Yang, X. Feng, *Angew. Chem., Int. Ed.* **2021**, *60*, 8689.

[46] C. B. Cockreham, C. B. Cockreham, X. Zhang, H. Li, E. H. Pereira, J. Sun, S. R. Saunders, Y. Wang, H. Xu, D. Wu, *ACS Appl. Energy Mater.* **2019**, *2*, 8145.

[47] G. S. Lee, T. Yun, H. Kim, I. H. Kim, J. Choi, S. H. Lee, H. J. Lee, H. S. Hwang, J. G. Kim, D. W. Kim, H. M. Lee, C. M. Koo, S. O. Kim, *ACS Nano* **2020**, *14*, 11722.

[48] B. Anasori, Y. Xie, M. Beidaghi, J. Lu, B. C. Hosler, L. Hultman, P. R. C. Kent, Y. Gogotsi, M. W. Barsoum, *ACS Nano* **2015**, *9*, 9507.

[49] Y. Xie, P. R. C. Kent, *Phys. Rev. B* **2013**, *87*, 235441.

[50] J. L. Hart, J. L. Hart, K. Hantanasirisakul, A. C. Lang, B. Anasori, D. Pinto, Y. Pivak, J. T. V. Omme, S. J. May, Y. Gogotsi, M. L. Taheri, *Nat. Commun.* **2019**, *10*, 522.

[51] H. Liu, Y. Liu, D. Zhu, *J. Mater. Chem.* **2011**, *21*, 3335.

[52] J. Halim, E. J. Moon, P. Eklund, J. Rosen, M. W. Barsoum, T. Ouisse, *Phys. Rev. B* **2018**, *98*, 104202.

[53] H. Kim, B. Anasori, Y. Gogotsi, H. N. Alshareef, *Chem. Mater.* **2017**, *29*, 6472.

[54] M. Ghidiu, S. Kota, J. Halim, A. W. Sherwood, N. Nedfors, J. Rosen, V. N. Mochalin, M. W. Barsoum, *Chem. Mater.* **2017**, *29*, 1099.

[55] E. S. Muckley, M. Naguib, H. W. Wang, L. Vlcek, N. C. Osti, R. L. Sacci, X. Sang, R. R. Unocic, Y. Xie, M. Tyagi, E. Mamontov, K. L. Page, P. R. C. Kent, J. Nanda, I. N. Ivanov, *ACS Nano* **2017**, *11*, 11118.

[56] J. Halim, J. Halim, M. R. Lukatskaya, K. M. Cook, J. Lu, C. R. Smith, L.-Å. Näslund, S. J. May, L. Hultman, Y. Gogotsi, P. Eklund, M. W. Barsoum, *Chem. Mater.* **2014**, *26*, 2374.

[57] S. A. Sergiienko, D. M. Tobaldi, L. Lajaunie, D. V. Lopes, G. Constantinescu, A. L. Shaula, N. D. Shcherban, V. I. Shkepu, J. J. Calvino, J. R. Frade, J. A. Labrinchaa, A. V. Kovalevsky, *J. Mater. Chem. C* **2022**, *10*, 626.

[58] K. Wang, Y. Zhou, W. Xu, D. Huang, Z. Wang, M. Hong, *Ceram. Int.* **2016**, *42*, 8419.

[59] E. Choi, J. Lee, Y. J. Kim, H. Kim, M. Kim, J. Hong, Y. C. Kang, C. M. Koo, D. W. Kim, S. J. Kim, *Carbon N Y* **2022**, *191*, 1.

[60] T. Habib, X. Zhao, S. A. Shah, Y. Chen, W. Sun, H. An, J. L. Lutkenhaus, M. Radovic, M. J. Green, *npj 2D Mater. Appl.* **2019**, *3*, 8.

[61] O. Mashtalir, K. M. Cook, V. N. Mochalin, M. Crowe, M. W. Barsoum, Y. Gogotsi, *J. Mater. Chem. A* **2014**, *2*, 14334.

[62] A. Favron, E. Gaufrès, F. Fossard, A. L. P. L 'Heureux, N. Y-W. Tang, P. L. Lévesque, A. Loiseau, R. Leonelli, S. Francoeur, R. Martel, *Nat. Mater.* **2015**, *14*, 826.

[63] D. Hanlon, C. Backes, E. Doherty, C. S. Cucinotta, N. C. Berner, C. Boland, K. Lee, A. Harvey, P. Lynch, Z. Gholamvand, S. Zhang, K. Wang, G. Moynihan, A. Pokle, Q. M. Ramasse, N. McEvoy, W. J. Blau, J. Wang, G. Abellan, F. Hauke, A. Hirsch, S. Sanvito, D. D. O'Regan, G. S. Duesberg, J. N. Coleman, *Nat. Commun.* **2015**, *6*, 8563.

[64] T. Wu, P. R. C. Kent, Y. Gogotsi, D. E. Jiang, *Chem. Mater.* **2022**, *34*, 4975.

[65] F. M. Römer, U. Wiedwald, T. Strusch, J. Halim, E. Mayerberger, M. W. Barsoumb, M. Farle, *RSC Adv.* **2017**, *7*, 13097.

[66] M. Han, X. Yin, H. Wu, Z. Hou, C. Song, X. Li, L. Zhang, L. Cheng, *ACS Appl. Mater. Interfaces* **2016**, *8*, 21011.

[67] D. D. L. Chung, Electromagnetic interference shielding effectiveness of carbon materials, **2001**.

[68] A. Iqbal, J. Kwon, M. K. Kim, C. M. Koo, *Mater. Today Adv.* **2021**, *9*, 100124.

[69] H. Bin Zhang, Q. Yan, W. G. Zheng, Z. He, Z. Z. Yu, *ACS Appl. Mater. Interfaces* **2011**, *3*, 918.

[70] A. Ameli, M. Nofar, S. Wang, C. B. Park, *ACS Appl. Mater. Interfaces* **2014**, *6*, 11091.

[71] M. H. Al-Saleh, W. H. Saadeh, U. Sundararaj, *Carbon* **2013**, *60*, 146.

[72] KEYSIGHT, https://www.keysight.com, (accessed: December 2023).

[73] K. Tserpes, V. Tzatzadakis, J. Bachmann, *J. Compos. Sci.* **2020**, *4*, 28.

2400024 (12 of 12)